Instabilities of a three-dimensional localized spot

Marcin Leda, Vladimir K. Vanag, and Irving R. Epstein
Department of Chemistry and Volen Center for Complex Systems, MS 015, Brandeis University, Waltham, Massachusetts 02454-9110, USA
(Received 26 August 2009; published 10 December 2009)

We investigate the behavior of localized spots in three spatial dimensions in a model two-variable system describing the Belousov-Zhabotinsky reaction in water-in-oil microemulsion. We find three types of instabilities: splitting of a single spot (i) into two spots, (ii) into a torus, and (iii) into an unstable shell that splits almost immediately to six or eight new spots.

DOI: 10.1103/PhysRevE.80.066204 PACS number(s): 89.75.Kd, 82.40.Ck, 82.20.−w, 47.57.jb

I. INTRODUCTION

In general, instabilities such as the Turing or wave instability can be classified as either supercritical or subcritical. In reaction-diffusion systems, supercritical instabilities of a homogeneous steady state (SS) can give rise to small-amplitude patterns, while subcritical instabilities are able to produce large-amplitude structures that can survive far from the bifurcation point [1]. In the case of subcritical instability, there is typically a range of parameters in which the homogeneous SS and a patterned state can coexist, with the homogenous SS remaining stable to small-amplitude spatial perturbations, while large-amplitude perturbations can induce patterns.

Localized spots are one example of such large-amplitude structures [2]. They may be stationary, traveling (stationary in a moving coordinate system) [3,4], or oscillatory (oscillons) [1]. Their profile does not depend on either the shape of the system or its size as long as the system dimensions are much larger than the width of a spot. To produce a localized spot from a stationary homogeneous SS, one must apply a finite perturbation of sufficient amplitude and appropriate shape. Usually the extent and shape of the perturbation should be comparable to those of the spot. Perturbations that do not have the correct size and shape decay, and the system comes back to the SS. Quasi-two-dimensional (quasi-2D) localized spots, both stationary and oscillatory, have been observed experimentally in the Belousov-Zhabotinsky (BZ) reaction in water-in-oil microemulsion [1,5]. This system is often referred to as the BZ-aerosol OT (AOT) system, where AOT is the common name for the surfactant, sodium bis(2-ethylhexyl) sulfosuccinate, used for preparation of the microemulsion.

Localized dissipative spots can be used for creating memory devices [6,7] since they can store information in much the same manner as an electronic memory, though they require a flow of fresh reactants to sustain them. For this reason, and because of the inherent interest of localized patterns, it is important to understand the stability properties of localized spots in both two- and three-dimensional (3D) systems. The case of three dimensions is especially interesting since the information capacity of such a chemical memory in three dimensions is significantly larger than in two dimensions.

Instabilities of large-amplitude patterns such as localized spots, Turing patterns, or traveling waves (planar or circular) are a productive source of new patterns. For example, continuous waves emitted when Turing spots in the chlorine dioxide-iodine-malonic acid (CDIMA) reaction become unstable produce segmented waves and eventually spatiotemporal chaos [8]. Instabilities of the planar or spiral 2D waves observed in the BZ-AOT system lead to stable dash waves [9].

By their nature, localized structures are ideally suited to the creation and control of stationary structures of various shapes [6], in particular those which lack symmetry. They may also be important in understanding morphogenetic processes in biological development.

Simulation of 3D patterns can be quite time consuming, and there is only a limited number of works in which 3D patterns have been studied [10–22]. Instabilities of 2D and 3D cylindrically and spherically symmetric localized patterns with sharp boundaries have been investigated by linear stability analysis for a generic two-activator-inhibitor reaction-diffusion system [23–25]. Here we focus on patterns arising from instabilities of a localized spot in the 3D domain using a two-variable model of the BZ-AOT system. Stationary 2D localized spots in this model have been studied previously by both numerical simulation [6] and linear stability analysis [26].

We choose the BZ-AOT system (and the corresponding model) because this is the most promising reaction-diffusion system for generating stationary 3D patterns. We have already observed 3D dash waves and Turing patterns visually in our laboratory, but we are still working to develop a viable method to reconstruct the 3D patterns from the complex 2D images we have obtained. Such systems as the CDIMA or ferrocyanide-iodide-sulfite [27] reactions, which are able to produce patterns in a thin quasi-2D gel layer in a continuously fed unstirred reactor, require continuous feeding, which is difficult to implement in a 3D configuration. The classic BZ reaction in aqueous solution is a good system for studying 3D scroll waves or spatiotemporal chaotic waves [28–31], but stationary 3D patterns have not been observed in this system, and, because the key species have very similar diffusion coefficients, it seems unlikely that they will be.

In Sec. II, we describe our model. Then in Sec. III we explain our methods: numerical simulation and linear stability analysis of a localized spot. In Sec. IV, we present our results, including separate investigations of cylindrically and spherically symmetric solutions. We conclude with Sec. V, where we compare our results for a localized 3D spot to the

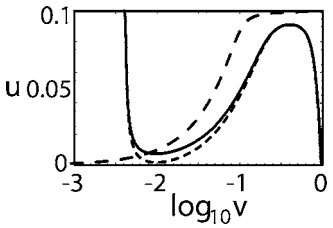

FIG. 1. Nullclines $dv/dt=0$ (solid and dotted lines) and $du/dt=0$ (dashed line) for system (1) at $m=10$, $f=1.85$, $q=0.004$, $\varepsilon_1=0.02$, and $i_0=0.01$ (solid line) and 0.02 (dotted line). Note that the horizontal axis has a logarithmic scale.

analogous results in two dimensions and extrapolate our findings to 3D Turing patterns as well.

II. MODEL

Our Oregonator-based model (1) belongs to a broad class of activator-inhibitor models. It can reproduce many of the 2D spatial structures observed in the BZ-AOT system: Turing patterns and large-amplitude patterns emerging from instabilities of planar, circular, and spiral waves and stationary localized spots [5,6]. The model equations are

$$\frac{\partial v}{\partial t}=\frac{1}{\varepsilon}\left([fu+i_0(1-mu)]\frac{q-v}{q+v}+v\frac{1-mu}{1-mu+\varepsilon_1}-v^2\right)+\Delta v, \tag{1a}$$

$$\frac{\partial u}{\partial t}=v\frac{1-mu}{1-mu+\varepsilon_1}-u+d\Delta u, \tag{1b}$$

where v (activator) is the dimensionless concentration of bromous acid $HBrO_2$ and u (inhibitor) is that of the oxidized form of the catalyst. We will assume that the catalyst is the photosensitive complex $[Ru(bpy)_3]^{3+}$, where bpy=2,2′-bipyridine.

In this study, we fix the parameters m, f, q, and ε_1 at the values used previously for the 2D case [6] ($m=10$, $f=1.85$, $q=0.004$, and $\varepsilon_1=0.02$). For these parameter values, the zero-dimensional (0D) version of Eq. (1) (without diffusion terms) has only one SS, which lies close to the fully reduced state of the catalyst. We will vary the parameters i_0, ε, and d. We choose i_0, which corresponds to the light intensity, to lie in the interval [0.005, 0.06]. For i_0 greater than 0.06, localized spots emerge at too large a value of d to be experimentally plausible. In the chosen interval, the SS is stable and excitable (see nullclines in Fig. 1). The threshold of excitability of system (1) is given approximately by the length of the horizontal interval between the SS and the middle branch of the v nullcline (solid and dotted lines in Fig. 1). The system is less excitable (the threshold of excitation is greater) for larger i_0 (see Fig. 1) and larger ε. We vary ε, which is a function of the rate constants and the concentrations of the BZ reactants [6], malonic acid, sulfuric acid, and bromate, between 0.1 and 1. In the classic aqueous BZ reaction, ε usually takes much smaller values, but for model (1) of the BZ-AOT system, this range of ε is reasonable. The ratio of diffusion coefficients $d=D_u/D_v$ is varied between 1 and 50 [localized spots and Turing instabilities can appear in model (1) only for $d>1$].

Setting the catalyst diffusion coefficient, D_u, larger than that of $HBrO_2$, D_v, may seem counterintuitive. However, as noted earlier, in this two-variable activator-inhibitor model, the catalyst plays the role of the inhibitor. It therefore adopts the diffusion rates of the actual inhibitors, Br^- and Br_2. In the BZ-AOT system, the diffusion rate of Br_2, w, a species soluble in the oil phase, is much larger than the diffusion rate of $HBrO_2$, a species that resides in the large water droplets. The ratio $D_u>D_v$ can be deduced from a more general model that was used to describe packet waves in the BZ-AOT system [32],

$$\frac{\partial v}{\partial \tau}=\frac{1}{\varepsilon_3}\left([fu+i_0(1-mu)]\frac{q-v}{q+v}+v\frac{1-mu}{1-mu+\varepsilon_1}-v^2\right)+D_v\Delta v, \tag{2a}$$

$$\frac{\partial u}{\partial \tau}=v\frac{1-mu}{1-mu+\varepsilon_1}-u-\alpha u+\gamma w+D_u\Delta u, \tag{2b}$$

$$\frac{\partial w}{\partial \tau}=(\alpha u-\gamma w)/\varepsilon_2+D_w\Delta w, \tag{2c}$$

where $D_w \gg D_v, D_u$. If w is a fast variable (which requires that $\gamma/\varepsilon_2 \gg 1+\alpha$), then we can assume quasiequilibrium for Eq. (2c) and write

$$w=(\alpha/\gamma)u. \tag{3}$$

Summing Eq. (2b) and ε_2 times (2c), we get

$$\frac{\partial(u+\varepsilon_2 w)}{\partial \tau}=v\frac{1-mu}{1-mu+\varepsilon_1}-u+D_u\Delta u+\varepsilon_2 D_w\Delta w, \tag{4}$$

and using Eq. (3), we finally obtain

$$\frac{\partial u}{\partial \tau}=\left(v\frac{1-mu}{1-mu+\varepsilon_1}-u\right)\Big/\left(1+\varepsilon_2\frac{\alpha}{\gamma}\right)+D_{u,eff}\Delta u, \tag{5}$$

where

$$D_{u,eff}=\left(D_u+\varepsilon_2\frac{\alpha}{\gamma}D_w\right)\Big/\left(1+\varepsilon_2\frac{\alpha}{\gamma}\right). \tag{6}$$

With the scaling of time and space as $\tau=(1+\varepsilon_2\alpha/\gamma)t$ and $x'=[D_v(1+\varepsilon_2\alpha/\gamma)]^{1/2}x$, we get Eqs. (1a) and (1b) from Eqs. (2a) and (5), where $d=D_{u,eff}/D_v$ and $1/\varepsilon=(1+\varepsilon_2\alpha/\gamma)/\varepsilon_3$. $D_{u,eff}$ is always greater than D_u if $D_w>D_u$. In our system, $D_w \gg D_u$, so $d>1$, since $D_v \cong D_u$.

III. METHODS

Now we return to system (1). We consider only parameter values d, i_0, and ε that do not give either a homogeneous SS (at any initial conditions) or a Turing instability. We solve system (1) numerically in a box of size $L_x \times L_y \times L_z$ with zero-flux (Neumann) boundary conditions (if $L_x=L_y=L_z$, we refer to this box as a 3D cubic domain). The values of L_x and L_y are always large compared to the radius R_S of a localized

spot, so that spot behavior is independent of L_x and L_y, while L_z is slightly (one to three times) larger than R_S in the case of cylindrically symmetric solutions to Eq. (1), and $L_z \gg R_S$ for spherically symmetric solutions. Our initial conditions are symmetric with respect to the center of the box,

$$v = v_p, \quad u = u_0 \quad \text{for} \quad r \le R_p$$

$$\text{and} \quad v = v_0, \quad u = u_0 \quad \text{for} \quad r > R_p, \tag{7a}$$

$$v = v_p, \quad u = u_0 \quad \text{for} \quad \rho \le R_p$$

$$\text{and} \quad v = v_0, \quad u = u_0 \quad \text{for} \quad \rho > R_p, \tag{7b}$$

where (v_0, u_0) is the homogenous SS, $r^2=(x-L_x/2)^2+(y-L_y/2)^2+(z-L_z/2)^2$ and $\rho^2=(x-L_x/2)^2+(y-L_y/2)^2$ in the case of spherically and cylindrically symmetric perturbations, respectively, v_p is the size of the perturbation, which exceeds the excitation threshold, and R_p is the radius of the perturbation. As a rule, the initial perturbation should have a radius comparable to that of a stationary localized spot. If R_p is significantly larger or smaller than R_S, the spot does not emerge from the homogeneous SS.

We solve system (1) numerically in the box domain using the finite difference, alternative direction, implicit (ADI) Crank-Nicolson algorithm [33] for the diffusion terms and the fourth-order Runga-Kutta algorithm for the kinetic terms. We employ a time step in the range $0.01 \le \Delta t \le 0.05$ and a spatial step $\Delta x = \Delta y = \Delta z$ between 0.1 and 0.2.

In addition to numerical integration of Eq. (1), we analyzed the stability of the cylindrically $[v_0(\rho), u_0(\rho)]$ and spherically $[v_0(r), u_0(r)]$ symmetric solutions of Eq. (1) by linear stability analysis in cylindrical (ρ, φ, z) and spherical (r, θ, φ) coordinate systems, respectively. The analysis, which is straightforward, is outlined in the supplementary information [34].

For the sake of simplicity, we use the term "nR solution" to signify the solution to Eq. (1) with only the radial part of the Laplacian in the cylindrical ($n=2$) and spherical ($n=3$) coordinate systems. We examine the stability of 2R and 3R solutions in cylindrical and spherical coordinate systems, respectively. Note that spherically symmetrical solutions can emerge in the system spontaneously (due to a large perturbation or a change in parameters), while cylindrically symmetric solutions can be generated, for example, with a perturbation by a narrow light beam.

IV. RESULTS

The simplest way to link a localized solution in two dimensions [6] to a related solution in three dimensions is to add an additional "vertical" axis (z) to the 2D system and analyze how the behavior of this spot as a cylindrically symmetric solution (2R) depends on the length of the z axis and the extent of the localized cylindrical perturbation. Figure 2 shows instabilities of such a localized cylinder $[v(x,y,z,t), u(x,y,z,t)] = [v(\rho,z,t), u(\rho,z,t)]$ in a box where $\rho^2=(x-L_x/2)^2+(y-L_y/2)^2$. For a sufficiently small height of the box, L_z, the 3D cylinder is stable [Fig. 2(a)]. If L_z increases, at a critical value of L_z ($L_{z\_cr} \cong 7.5$), the 3D cylinder becomes unstable and transforms to a hemisphere [Fig. 2(b)], the diameter of which coincides with either the upper or lower horizontal boundary. For larger L_z, the initial cylinder splits into a periodic structure, like that shown in Fig. 2(c), with several full spheres and two hemispheres. The number of spheres increases with L_z. The transient cylindrically symmetric structure shown in Fig. 2(c) is not stable and evolves in time into the stationary structure shown in Fig. 2(d). The spatial period Λ_p of such a structure can be defined as the z component of the distance between centers of neighboring spheres (or hemispheres). The structure in Fig. 2(d) is composed of two periods, while the structure in Fig. 2(b) contains only half a period. When we increase the diffusion parameter, d, a different instability of the 2R solution becomes possible for the same length L_z. For example, the transient structure shown in Fig. 2(e) does not have cylindrical symmetry and continues to evolve into one sphere and two hemispheres [see Fig. 2(f)], as in the previous case for smaller values of d. But here, the structure shown in Fig. 2(f) is not stationary and undergoes further transformation. Each sphere and hemisphere splits in two. These splittings continue until the entire spatial domain is occupied by balls (all hemi-

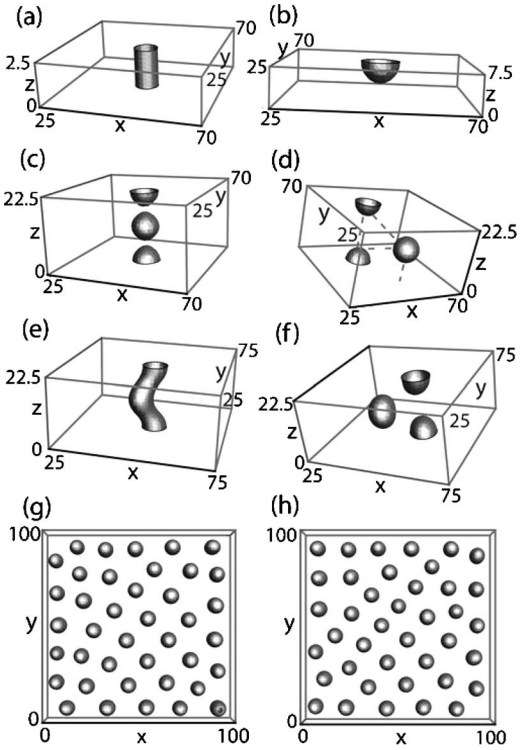

FIG. 2. Instabilities of localized cylindrical solutions in 3D box domains. Isosurfaces shown correspond to $u=0.04$. (a) Stationary localized cylinder, $L_z=2.5$. (b) Stationary localized hemisphere, $L_z=7.5$. (c) Transient structure at $t=100$, $L_z=22.5$. (d) Stationary localized pattern evolving from (c), $t=1200$. (e) and (f) Transient structures at $t=$(e) 208 and (f) 240; $L_z=22.5$. (g) and (h) Stationary pattern evolving from (f) $t=1200$ [(g) lower layer $0<z<L_z/2$; (h) upper layer $L_z/2<z<L_z$]. Parameters: $\varepsilon=0.4$, $i_0=0.01$, $d=$(a)–(d) 10 and (e)–(h) 20. Note that only the central portion of the x-y domain with $L_x=L_y=95$ is shown. Lengths and times are given in dimensionless units.

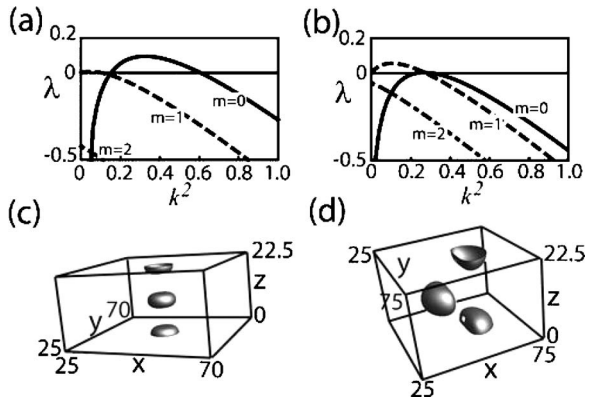

FIG. 3. (a) and (b) Dispersion curves for the cylindrically symmetric solution for $m=0,1,2$, $d=$(a) 10 and (b) 20. (c) and (d) Eigenfunctions δu corresponding to the maximum of the curve in (c) (a) for $m=0$ ($k^2=0.31$) and (d) (b) for $m=1$ ($k^2=0.11$). Isosurfaces correspond to $\delta u=0.1$. Parameters $\varepsilon=0.4$, $i_0=0.01$.

spheres eventually transform to spheres). The stationary solution is composed of two layers of spheres. Figures 2(g) and 2(h) show the lower and upper layers, respectively. Both layers are slightly irregular since the number of nearest neighbors in a horizontal layer ranges from 4 to 6. We have not investigated the symmetry of the final Turing patterns in this situation.

The dispersion curve in Fig. 3(a) (solid line) shows that a 2R spot is unstable with respect to axial perturbations [$m=0$, where the solutions are proportional to $\exp(im\varphi)$] at axial wave numbers $k^2 \in (0.15, 0.6)$. The wave number $k_{\max}$, corresponding to the maximum of this curve (close to $k^2=0.31$), determines the spatial period Λ_p as $\Lambda_p \cong 2\pi/k_{\max}$ ($\cong 11.3$). The critical value L_{z_cr} can be found approximately as $2\pi/k_1$, where k_1 is the wave number at which the eigenvalue λ (at $m=0$) changes sign from positive to negative ($k^2 \cong 0.6$). The eigenfunction shown in Fig. 3(c) corresponds to the maximum in the dispersion curve with $m=0$ [solid line in Fig. 3(a)], i.e., this cylindrically symmetric solution, with period Λ_p, should grow faster than other cylindrical symmetric perturbations. In Fig. 2(c), we see such a cylindrically symmetric perturbation with period $\Lambda_p=L_z/2$. The dispersion curve for angular perturbations with $m=1$ [dotted line in Fig. 3(a)] has a smaller maximum, which is moreover shifted to greater periods Λ_p. Hence, such perturbations can develop only for larger L_z but grow more slowly than perturbations with $m=0$. Angular perturbations with $m=2$ [dotted-dashed line in Fig. 3(a)] always decay to zero because their eigenvalues are negative at all k.

The 2R solution may also be unstable to angular perturbations. For larger d, the maximum in the dispersion curve for angular perturbations with $m=1$ is greater than that for cylindrically symmetric perturbations ($m=0$) [see Fig. 3(b)]. Hence, the eigenfunction shown in Fig. 3(d), which is associated with the dispersion curve maximum for $m=1$ in Fig. 3(b) should correspond to the perturbation with the fastest rate of growth. We see such a developing perturbation in the numerical simulation in Fig. 2(e). As in the previous case, all angular perturbations for $m=2$ disappear since the corresponding eigenvalues [dispersion curve and dotted-dashed line shown in Figs. 3(a) and 3(b)] assume only negative values.

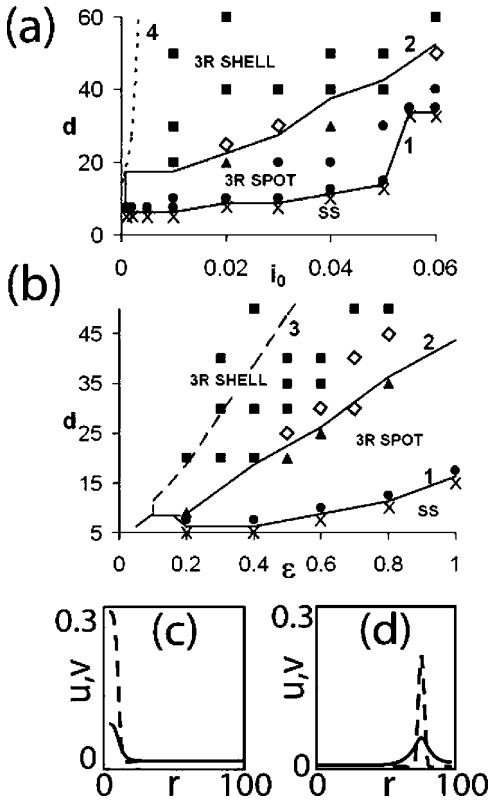

FIG. 4. Parametric diagrams for system (1) for (a) $\varepsilon=0.4$ and (b) $i_0=0.01$. Dashed line 4 in (a) is the onset of Turing instability. Dashed line 3 in (b) shows the boundary between a cylindrically symmetric stationary localized spot and a cylindrically symmetric stationary ring found by linear stability analysis in three dimensions. Solid lines 1 and 2 correspond to the spherically symmetric solution. Lines 2 in (a) and (b) separate spherically symmetrical solutions "3R shell" and "3R spot" found by linear stability analysis in three dimensions. Lines 1 in (a) and (b) separate domains of homogeneous SS and localized spots found numerically by simulations in a 3D box. Abbreviations: "SS"=homogeneous SS, 3R spot=spherically symmetric localized stationary spot around $r=0$ [shown in (c)], and 3R shell=stationary spherically symmetric shell close to $r=R$ [shown in (d), where $R=100$]. Symbols correspond to patterns found in 3D box domain: open circles—3D localized stationary spot, diamond—splitting of a spot to torus [shown below in Figs. 6(d)–6(f)], triangles—splitting of a spot to two spots [shown below in Figs. 6(a)–6(c)], and squares—splitting of a spot to a shell, which immediately splits to six [Fig. 7(b)] or eight [Fig. 7(f)] spots. (c) and (d) Profiles of v (dashed line) and u (solid line) for stationary localized spherically symmetric solutions of system (1) at $i_0=0.01$, $\varepsilon=0.4$, and $d=$(c) 10 and (d) 20.

Our main results on the stability of a 3D localized spherical spot in system (1) are summarized in Fig. 4. Lines 1 in Figs. 4(a) and 4(b) separate domains of the homogeneous SS and localized stationary spots found in numerical simulations of system (1) in a 3D box (with large L_x, L_y, and L_z). Solutions with a stationary localized spot are marked by solid circles in Figs. 4(a) and 4(b), while the homogeneous SS is marked by crosses. A typical 3D spot localized in the center of a box or in the center of a 3D ball with radius R (3R spot)

[see Fig. 4(c)] has width at half height ≅4. Note that a stationary spot does not emerge if the radius of perturbation $R_p > 6$ (at our chosen parameters). Localized spots (3R spots) can be found, in general, only between lines 1 and 4 in Fig. 4(a), where the dotted line 4 in Fig. 4(a), the onset of Turing instability, was obtained analytically by linear stability analysis in one dimension. Above and to the left of this line, the stationary state is unstable to infinitesimal spatial perturbations. The domain of stationary localized spots actually occupies only part of the region between lines 1 and 4 due to the instabilities of a localized spot. The Turing instability area bounded by line 4 is not shown in Fig. 4(b) because it exists only above $d=100$, which cannot be achieved experimentally.

A localized spot can lose stability if a parameter of system (1) changes. For example, a spot can emit a 3D wave if d exceeds a critical value. This bifurcation is due to a radial instability. In an infinite domain, a traveling 3D spherical wave, which looks like a growing 3R shell, is the asymptotic solution. However, in a finite spherically symmetrical system, this 3D wave stops close to the spherical boundary and forms a stationary spherically symmetrical shell [shown in Fig. 4(d)]. To find the border in the parameter space between these two spherically symmetrical solutions (localized spot and shell), we performed linear stability analysis of a 3R localized spot. The result of this analysis is shown by line 2 in Figs. 4(a) and 4(b). Analogous to the spot-shell transition in a spherically symmetric spatial domain, a 2R spot in a cylindrically symmetrical spatial domain can lose stability by emitting a cylindrically symmetric 3D propagating wave that stops close to the boundary and forms a stationary "2R shell" or, more accurately, a "2R ring." The onset of this instability, obtained by linear stability analysis for radial perturbations in a cylindrically symmetrical system, is shown by dashed line 3 in Fig. 4(b) [the analogous line in Fig. 4(a) is not shown].

A spherically symmetric localized spot may also be unstable to angular perturbations, characterized by the indices l and m (see Ref. [34]). Patterns emerging due to such perturbations and found numerically in a 3D box are marked by triangles, squares, and rhombs in Figs. 4(a) and 4(b). If a 3R spot is stable to all infinitesimal perturbations, we call it a 3D localized spot [marked by circles in Figs. 4(a) and 4(b)]. We discuss these solutions below.

We now compare 3R localized stationary spots [shown in Fig. 4(c)] and 2R localized stationary spots [shown in Fig. 2(a)]. First, the amplitude (the maximum values of u and v) of the 3R spot is greater [see projections of concentration profiles on the (v,u) plane in Fig. 5]. Moreover, the transition from 2R spot to 2R ring [dashed line 3 in Fig. 4(b)] occurs at higher values of d than in the case of 3R spots [line 2 in Fig. 4(b)]. The stability curve separating the 3R spot and 3R shell solutions (line 2) is well approximated by $d_{cr} \propto 44\varepsilon_{cr}$ (for $i_0=0.01$) in Fig. 4(b). For greater i_0, the slope is greater (70 for $i_0=0.03$) because d_{cr} increases when i_0 increases [line 2 in Fig. 4(a)]. The corresponding line for 2R spots [line 3 in Fig. 4(b)] has a larger slope, $d_{cr} \propto 96\varepsilon_{cr}$, i.e., the spherically symmetric shell appears for smaller values of d than the cylindrically symmetric ring when the other parameters are the same. If we consider only radial perturbations, then for a given set of parameters we see following sequence of solutions: SS→3R spot→3R shell as d increases [Fig. 4(a) and 4(b)].

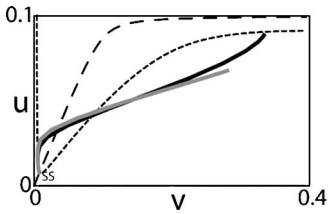

FIG. 5. Projections of cylindrically 2R (gray) and spherically 3R (black) symmetric spots on the (v,u) plane. Parameters: $i_0=0.01$, $\varepsilon=0.4$. Dotted and dashed lines are nullclines, where dv/dt or $du/dt=0$ in the 0D system for the activator and the inhibitor, respectively. The upper end of each projection corresponds to concentrations at $r=0$ and the lower end to $r=100$, where the system is in the SS.

As noted above, a localized spot can be unstable to angular perturbations as well. The three main types of localized spot instabilities we found in our simulations in a 3D cubic domain are due to these angular perturbations. They are

(i) spot splitting to two spots [marked by triangles in Figs. 4(a) and 4(b); see also Fig. 6(a)],

(ii) spot deforming to a torus [diamonds in Figs. 4(a) and 4(b); see also Fig. 6(d)], and

(iii) spot deforming to a spherically symmetric shell that immediately splits to six or eight spots [squares in Figs. 4(a)

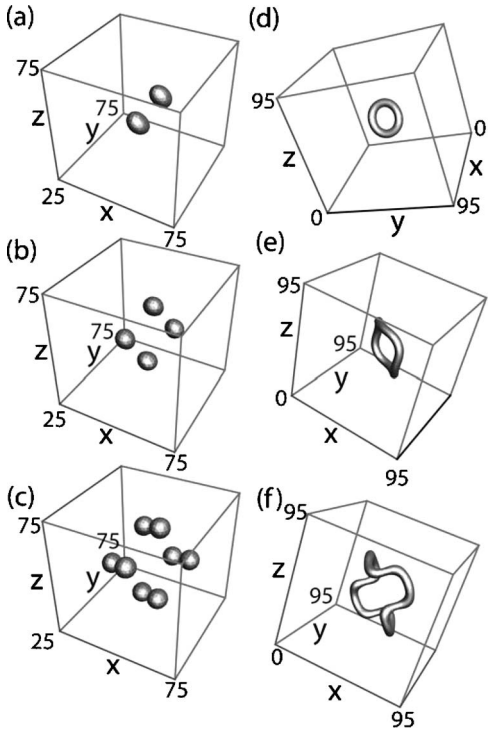

FIG. 6. Splitting of 3D localized spot in a cubic domain, $L_x=L_y=L_z=95$, for (a)–(c) $i_0=0.02$, $d=20$ and (d)–(f) $i_0=0.03$, $d=30$ at $t=$(a) 120, (b) 150, (c) 180, (d) 150, (e) 270, and (f) 330. Note that only part of the computational domain is shown in (a)–(c). Isosurfaces shown correspond to $u=0.06$. $\varepsilon=0.4$.

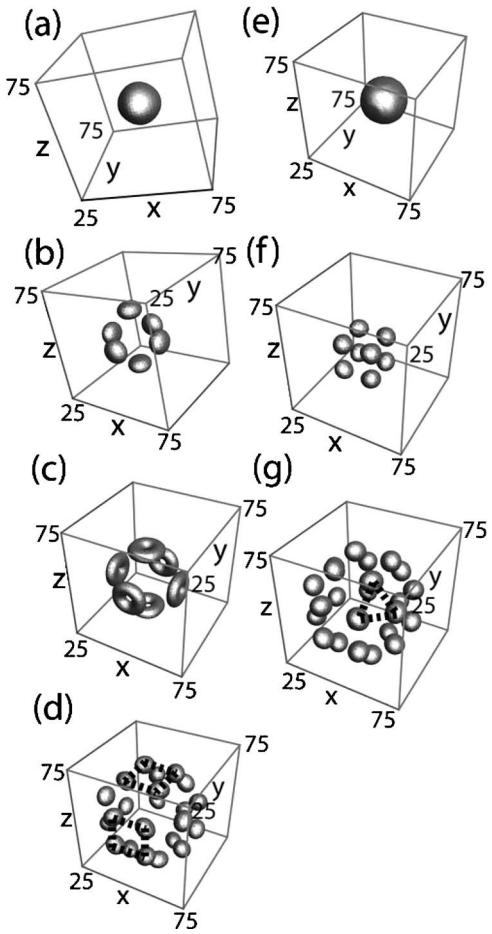

FIG. 7. Splitting of 3D localized spot in 3D cube domain $L_x=L_y=L_z=95$ for (a)–(d) $i_0=0.01$, $d=20$ and (e)–(g) $i_0=0.04$, $d=40$ at $t=$(a) 62.5, (b) 75, (c) 100, (d) 150, (e) 62.5, (f) 125, and (g) 250. Only part of the computational domain is shown. Isosurfaces correspond to $u=0.06$. $\varepsilon=0.4$.

and 4(b); see also Figs. 7(a) and 7(b) and Figs. 7(e) and 7(f), respectively]. In Figs. 6 and 7, we present and analyze in detail these three instabilities.

Case (*i*). As in 2D systems [6,26], we observe a spot splitting to two spots (replication). In Figs. 6(a)–6(c), three consecutive replications are shown in the 3D domain. The initial spot splits to two spots along the direction of replication [Fig. 6(a)]. The next splitting gives four coplanar spots and takes place perpendicular to the direction of the first replication step [Fig. 6(b)]. The direction of the third splitting is perpendicular to the plane of the first two, yielding a cuboid composed of eight spots [Fig. 6(c)].

Case (*ii*). In the 3D domain we also observe a spot deforming to a torus [Fig. 6(d)], which is unstable. After some time it forms a folded ring-shaped continuous structure [Fig. 6(e)], which deforms further [Fig. 6(f)] and persists until it approaches the domain walls. Then the structure stops and breaks into spots.

Case (*iii*). A localized spot may deform to a 3R shell [Figs. 7(a) and 7(e)], as can be seen, for example, in the plane $x=L_x/2$ [Figs. 8(a) and 9(a)] or the plane $x=y$ [Figs. 8(c) and 9(d)]. In all our simulations, the shell was also unstable and split almost immediately to six [octahedron, Fig.

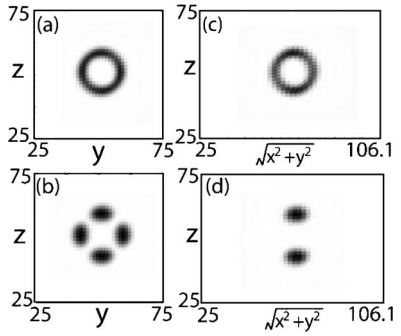

FIG. 8. 2D cross sections of 3D solutions shown in Figs. 7(a) and 7(b) made across the planes (a) and (b) $x=L_x/2$ and (c) and (d) $x=y$. Dark areas correspond to large concentrations of activator v.

7(b)] or eight [cube, Fig. 7(f)] spots. Splitting to six spots can be viewed as a ring splitting to four spots in each plane, $x=L_x/2$, $y=L_y/2$, and $z=L_z/2$ [in Fig. 8(b) we show only the plane $x=L_x/2$], and to two spots in the diagonal plane, $x=y$ [Fig. 8(d)]. The dynamics of spot splitting into eight spots (at $t=125$) is illustrated in Fig. 9. In Fig. 9(b), in the plane $x=L_x/2$, we show splitting to four spots at $t=72.5$ and then [Fig. 9(c)], at $t=75$, the vanishing of these spots. In the diagonal plane $x=y$, the shell splits to two half-circles [Fig. 9(e)] and then each of the half-circles splits to two spots [Fig. 9(f)].

Figures 7(c) and 7(d) show the further evolution of the six-spot pattern shown in Fig. 7(b). Each of the six spots deforms to a toroidal structure [Fig. 7(c)], and then each

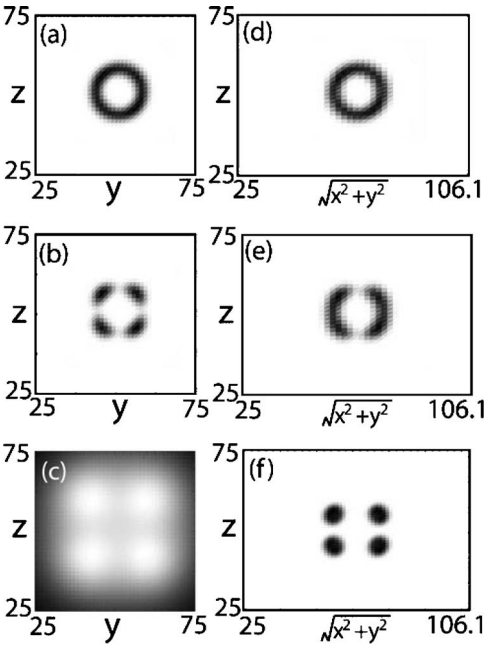

FIG. 9. 2D cross sections of 3D solutions at $t=$(a) and (d) 62.5, (b) and (e) 72.5, and (c) and (f) 250 in the planes (a)–(c) $x=L_x/2$ and (d)–(f) $x=y$. Panels (a) and (d) correspond to Fig. 7(e) and panels (c) and (f) to Fig. 7(f). Dark areas correspond to large concentrations of activator v. Note that the gray scale in panel (c) is 100 times finer than in the other panels (black and white areas correspond to values $v\approx0.0049$ and $v\approx0.0044$, respectively).

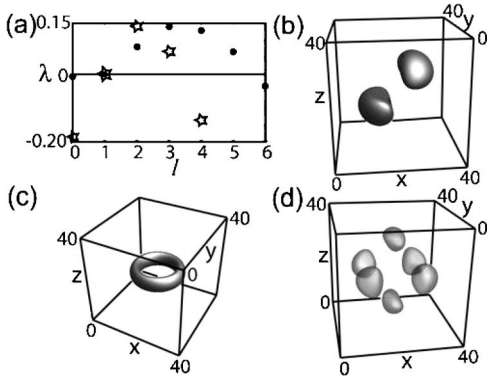

FIG. 10. (a) Dispersion curves for spherically symmetric solutions at $i_0=0.01$, $d=17$ (stars) and $i_0=0.05$, $d=41$ (solid circles), $\varepsilon=0.4$. Eigenfunctions δu for (b) $l=2$, $m=1$, (c) $l=2$, $m=0$, and (d) $l=4$, $m=2$. Isosurfaces shown in (b)–(d) correspond to $\delta u=$(b) and (c) 0.1 and (d) 0.6.

toroid splits into four spots, giving a 24-spot pattern [Fig. 7(d)]. Spots appearing as a result of the splitting of two of the toroids are marked with dashed trapezoids in Fig. 7(d).

Figure 7(g) shows the further evolution of the eight-spot pattern shown in Fig. 7(f). Each of the eight spots splits into three spots. The spots originating from one chosen spot are marked with a dashed triangle in Fig. 7(g). After three steps of splitting, we recognize a 24-spot pattern [Fig. 7(g)] with the same symmetry (and nearly the same locations of spots) as the pattern shown in Fig. 7(d).

All the instabilities observed in our numerical simulations can be identified by linear stability analysis. The dispersion curves in Fig. 10(a) show that a localized spot is stable to radial perturbation, since $\lambda<0$ at $l=0$, but unstable to angular perturbations with $1\leq l\leq 5$. The eigenvalue λ is negative at $l=0$, but its absolute value is very small at our chosen parameters i_0, d, and ε, where system (1) is very close to the boundary between the 3R localized spot and the 3R traveling shell [lines 2 in Figs. 4(a) and 4(b)]. This choice allows us to predict the symmetry of the instability of traveling 3R shells close to this boundary as well. In Figs. 10(b)–10(d) we present eigenfunctions for several values of m and l at which λ is positive. They correspond to a localized spot splitting to two spots ($l=2$, $m=1$), torus ($l=2$, $m=0$), and six spots ($l=4$, $m=2$), respectively. In Fig. 10(a), we see that the maximum in the dispersion curve shifts from $l=2$ (stars) toward $l=4$ (solid circles) when d is increased. This result implies that at small values of d we should observe splitting to two spots or a torus, while for larger d splitting to six spots should occur, a sequence found in our numerical simulations [see patterns along the vertical line $i_0=0.02$ in Fig. 4(a)].

V. DISCUSSION AND CONCLUSION

Using model (1) for the BZ-AOT system, we have found several types of instabilities of a localized spot in three dimensions, namely, transformation of a spot (i) to two spots, (ii) to a torus, and (iii) to an unstable shell that splits almost immediately to six or eight spots. In case (ii), the torus increases in diameter and transforms to a folded continuous ring-shaped structure, which can be observed for a relatively long time before breaking into spots upon colliding with the boundary. In all three cases, the final stationary spotlike patterns occupy the entire area.

Instabilities of a localized spot, in general, are due to radial and angular perturbations. If we consider only radial perturbations (as in our linear stability analysis), then a spot should lose stability only above line 2 in Figs. 4(a) and 4(b). Indeed, we do not see black circles (stable spots) above this line, but we do see triangles and rhombs below it, which means that a localized spot can lose stability even below this line as a result of angular perturbations that produce instabilities of types (i) (triangles in Fig. 4) and (ii) (rhombs).

Instability of type (i) was also found in the case of 2D localized spots [6]. The distortion of a 2D spot into a circular wave has its analog in three dimensions in the form of instabilities, (ii) torus and (iii) shell-like unstable 3D wave. The latter instability can be considered an essentially new one since it results in splitting of a spot to six or eight new spots.

Our theoretical analysis, including the existence of eigenfunctions for different values of l and m, shows that other types of instabilities are also possible, but we have not observed these instabilities in our computer simulations. This question requires further investigation, but it seems likely that the basins of attraction of these instabilities are too small to be located in a computer experiment, at least in the parameter ranges we explored.

All three types of instabilities found in our computations can produce stationary Turing patterns with different symmetries. For the parameters used in this study, Turing patterns are composed of spots only. However, for larger values of ε and d (for example, $\varepsilon=0.4$, $d=40$, and $i_0=0$), Turing instability can produce stationary spherical shells. If system (1) has its stationary state close to the fully oxidized state of the catalyst (large parameter m), stationary Turing patterns can assume the shape of cylindrical shells and/or lamellar structures (for still larger d). Investigation (both theoretical and experimental) of these symmetries and their comparison to other symmetries of Turing patterns found in three dimensions [15,20,21,35,36] may be the subject of further work.

Localized patterns may be used for the production of custom asymmetric patterns or for memory devices [6]. The capacity of such a memory is limited by the width of a spot, which is proportional to $(D_u\varepsilon)^{1/2}$. Knowledge of the stability regions of localized stationary structures is necessary in constructing such devices.

Localized stationary patterns can also explain the development of morphogenetic patterns. They can be created only if the excitatory signal exceeds a threshold value. In this way, morphogenetic action can be limited to strictly controlled areas of a developing organism.

ACKNOWLEDGMENT

This work was supported by the National Science Foundation through Grant No. CHE-0615507.

[1] V. K. Vanag and I. R. Epstein, Phys. Rev. Lett. **92**, 128301 (2004).
[2] V. K. Vanag and I. R. Epstein, Chaos **17**, 037110 (2007).
[3] Y. Nishiura, T. Teramoto, and K. I. Ueda, Chaos **15**, 047509 (2005).
[4] Y. A. Astrov and H. G. Purwins, Phys. Lett. A **358**, 404 (2006).
[5] A. Kaminaga, V. K. Vanag, and I. R. Epstein, J. Chem. Phys. **122**, 174706 (2005).
[6] A. Kaminaga, V. K. Vanag, and I. R. Epstein, Angew. Chem., Int. Ed. **45**, 3087 (2006).
[7] P. Coullet, C. Riera, and C. Tresser, Chaos **14**, 193 (2004).
[8] L. F. Yang, I. Berenstein, and I. R. Epstein, Phys. Rev. Lett. **95**, 038303 (2005).
[9] V. K. Vanag and I. R. Epstein, Proc. Natl. Acad. Sci. U.S.A. **100**, 14635 (2003).
[10] S. Alonso, F. Sagués, and A. S. Mikhailov, Science **299**, 1722 (2003).
[11] S. Alonso, F. Sagués, and A. S. Mikhailov, J. Phys. Chem. A **110**, 12063 (2006).
[12] S. Alonso and A. V. Panfilov, Chaos **17**, 015102 (2007).
[13] P. Kettunen *et al.*, Chaos **16**, 037111 (2006).
[14] P. Kettunen *et al.*, Math. Comput. Modell. **41**, 1013 (2005).
[15] A. De Wit, G. Dewel, P. Borckmans, and D. Walgraef, Physica D **61**, 289 (1992).
[16] H. Shoji, K. Yamada, D. Ueyama, and T. Ohta, Phys. Rev. E **75**, 046212 (2007).
[17] H. Shoji and K. Yamada, Jpn. J. Ind. Appl. Math. **24**, 67 (2007).
[18] H. Shoji, K. Yamada, and T. Ohta, Phys. Rev. E **72**, 065202(R) (2005).
[19] T. K. Callahan and E. Knobloch, Phys. Rev. E **64**, 036214 (2001).
[20] T. K. Callahan and E. Knobloch, Physica D **132**, 339 (1999).
[21] A. De Wit, P. Borckmans, and G. Dewel, Proc. Natl. Acad. Sci. U.S.A. **94**, 12765 (1997).
[22] T. K. Callahan and E. Knobloch, Nonlinearity **10**, 1179 (1997).
[23] C. B. Muratov and V. V. Osipov, Phys. Rev. E **54**, 4860 (1996).
[24] C. B. Muratov, Phys. Rev. E **54**, 3369 (1996).
[25] C. B. Muratov and V. V. Osipov, Phys. Rev. E **53**, 3101 (1996).
[26] T. Kolokolnikov and M. Tlidi, Phys. Rev. Lett. **98**, 188303 (2007).
[27] K. J. Lee, W. D. McCormick, J. E. Pearson, and H. L. Swinney, Nature (London) **369**, 215 (1994).
[28] T. Amemiya *et al.*, Chaos **8**, 872 (1998).
[29] T. Bánsági and O. Steinbock, Phys. Rev. Lett. **97**, 198301 (2006).
[30] W. Jahnke, C. Henze, and A. T. Winfree, Nature (London) **336**, 662 (1988).
[31] C. Luengviriya, U. Storb, G. Lindner, S. C. Müller, M. Bär, and M. J. B. Hauser, Phys. Rev. Lett. **100**, 148302 (2008).
[32] V. K. Vanag and I. R. Epstein, Phys. Rev. Lett. **88**, 088303 (2002).
[33] C. A. J. Fletcher, *Computational Techniques for Fluid Dynamics* (Springer-Verlag, Berlin, 1991), Vol. 1.
[34] See EPAPS Document No. E-PLEEE8-80-072911 for the linear stability analysis in cylindrical and spherical coordinate systems. For more information on EPAPS, see http://www.aip.org/pubservs/epaps.html.
[35] T. K. Callahan, Physica D **188**, 65 (2004).
[36] T. Leppanen, M. Karttunen, R. A. Barrio, and K. Kaski, Phys. Rev. E **70**, 066202 (2004).